eMagRes
MRI | NMR

Direct Water–Fat Imaging Methods: Chemical Shift-Selective and Chemical Shift-Encoded MRI

Houchun Harry Hu[1] & Diego Hernando[2]

[1] *Phoenix Children's Hospital, Phoenix, AZ, USA*
[2] *University of Wisconsin-Madison, Madison, WI, USA*

This article summarizes direct imaging methods designed to separate water and fat signals in proton magnetic resonance imaging. The methods presented fundamentally rely on the difference in resonance frequencies between water (hydroxyl) and predominant fat (methylene) protons. The discussed techniques are divided into two categories, (i) RF-based approaches that selectively suppress or excite water and fat signals and (ii) multiecho imaging strategies that separate water and fat signals based on chemical shift-encoding. The various clinical utilities of these methods are detailed, from traditional fat suppression endpoints to more recent trends toward quantitative fat-fraction imaging. Comparative examples are illustrated, along with some discussion of the advantages and limitations of each method. In the context of quantitative fat imaging, the impact of modeling fat more realistically, as a multipeak triglyceride signal versus a traditional simplified single-methylene-peak representation, is highlighted, and similarly, the effects of confounding factors on quantitative accuracy and precision are summarized. Approaches to multiecho chemical shift-encoded data acquisitions and reconstructions are presented, and methodological considerations for echo-time selection and main magnetic field inhomogeneity are outlined. Finally, recent advances in chemical shift-encoded imaging toward the characterization of triglyceride properties (e.g., chain length and unsaturation degree) are briefly discussed.

Keywords: chemical shift-selective imaging, chemical shift-encoded imaging, Dixon imaging, proton-density fat fraction, fat suppression, fat quantification, multiecho imaging, signal fat fraction, water–fat separation, water excitation

How to cite this article:
eMagRes, 2015, Vol 4: 673–688. DOI 10.1002/9780470034590.emrstm1480

Introduction

This article's content was largely motivated by proceedings from the 2012 International Society for Magnetic Resonance (ISMRM) workshop on water–fat imaging (http://ismrm.org/workshops/FatWater12/).[1] The goal is to provide the reader with a concise overview of chemical shift-based water–fat proton magnetic resonance imaging (MRI) techniques, including chemical shift-selective (CHESS) and chemical shift-encoded (CSE) methods. Specifically, the article will describe how CSE water–fat imaging approaches fundamentally differ from traditional single-voxel magnetic resonance spectroscopy (MRS) and multivoxel chemical shift-imaging (CSI) (see ***CSI and SENSE CSI***; ***2D MRS***). As summarized in Table 1, CSE MRI methods can be considered as a subset of CSI approaches. Reconstruction of CSE water–fat MRI data is performed using well-defined spectral models, where strong constraints in the form of known chemical frequency shifts and relative amplitudes of the chemical species to be separated (e.g., water and fat) are established a priori. In contrast, the spectral model is less constrained in traditional CSI postprocessing algorithms. By exploiting this a priori knowledge of the water–fat spectral model, gains in both imaging speed and spatial resolution can be achieved with CSE imaging methods.

The article will highlight the clinical utility of chemical shift-based water–fat MRI techniques. Cartesian data sampling of *k*-space is considered herein, and the word 'fat' is used to denote triglyceride molecules. The section titled 'Chemical Shift-Selective Imaging' briefly summarizes conventional RF (transmit field, B_1)-based approaches that selectively suppress fat or excite water signals, and showcases examples where the uniform suppression of fat signals is critical to the diagnostic quality of the resultant clinical images. In the context of these discussions, a simplified two-peak water–fat spectral model is considered. In this simplified model, the triglyceride spectrum is represented only by its predominant methylene peak, which is 3.4 ppm downfield from the water resonance. For the purpose of fat suppression, this simplified model is adequate. Extensive reviews on CHESS approaches can be found in the literature.[2–5] For brevity, conventional spin lattice (T_1)-based water and fat-suppression methods based on inversion recovery[6] are not discussed here (see ***Tissue Water and Lipids: Chemical Shift Imaging and Other Methods***).

In the section titled 'Chemical Shift-Encoded Water–Fat Imaging', emphasis is given to multiecho CSE MRI, historically referred to as Dixon water–fat MRI. Over the past three decades since W. T. Dixon's seminal 1984 paper, there have been significant methodological advances and increased use of CSE MRI techniques in both research and clinical settings.[7,8]

Table 1. Fundamental differences between spectroscopy and chemical shift-encoded (CSE) water–fat MRI

	Spectroscopy		CSE MRI
	1-D single voxel MRS	2-D and 3-D CSI	
Spatial encoding (matrix size)	No	Yes (16 × 16 to 32 × 32)	Yes (256 × 256 to 512 × 512)
Spatial (voxel) resolution	Low (mm to cm)	Low (mm to cm)	High (sub-mm to mm)
Frequency (spectral) resolution	High	High	Low (predefined components)
Model based: A priori assumption of resonance frequencies and relative spectral peak areas of chemical species	Weak constraints	Weak constraints	Strong constraints (single and multipeak fat models)
Relative acquisition speed	Can be fast (depending on application)	Slow	Typically fast

Note the tradeoff between spectral and spatial resolutions.

We will discuss several technical considerations for CSE data acquisition and data reconstruction. While the original motivation for qualitative CSE was to achieve superior water–fat separation and fat suppression compared to CHESS techniques, the emerging concept of quantitative fat-fraction imaging from CSE MRI is highlighted (see ***Ultrafast Multidimensional NMR: Principles and Practice of Single-Scan Methods***). Quantitative fat-fraction imaging is becoming increasingly popular in obesity and metabolism research (see ***Body Fat Metabolism: Observation by MR Imaging and Spectroscopy***, ***Insulin resistance, type 2 diabetes and obesity and other metabolic disorders studied by MRS***, ***In Vivo MRS of Lipids in Adipose Tissue, Bone Marrow, and Liver***), either in conjunction with or in lieu of spectroscopy, to assess adipose tissue volume and triglyceride properties (see ***Body Fat MRS***) and ectopic fat content in the liver (see ***Monitoring Fatty Liver***), the heart (see ***Cardiac Lipids by ^1H MRS***), the pancreas, and the skeletal muscle (see ***Muscle studies by ^1H MRS***). In the context of quantitative imaging, and in the interest of improving the accuracy and reproducibility of fat-fraction estimates, a more general multipeak water–fat spectral model is considered, where the triglyceride spectrum is represented more realistically by multiple resonances (e.g., methyl, olefinic, carboxyl, and glycerol), in addition to the primary methylene component. The article will conclude with a brief outlook of future research directions in CSE MRI.

Chemical Shift-Selective Imaging

In CHESS MRI, magnetization preparation is achieved by spectrally selective RF pulses that either excite or suppress water or fat resonance frequencies before data acquisition (see ***Selective Excitation in MRI and MR Spectroscopy***). In one approach, spectral-spatial RF pulses are applied to selectively excite either the water or the methylene fat protons before data acquisition. The resultant image reflects signals only from the component that was spectrally excited. In another strategy, frequency-selective RF pulses are first applied to suppress signals from water or methylene protons. Subsequently, signals from the nonsuppressed component are acquired for image formation.[9–11] Some of the major advantages of CHESS techniques include their versatility in coupling to nearly all MRI pulse sequences, and their ease of implementation and availability on all commercial human MRI platforms.

Selective Fat Suppression

The suppression of typically hyperintense signals from fat in proton-density-weighted, spin–lattice relaxation (T_1)-weighted, and spin–spin relaxation (T_2)-weighted MRI images is routine in clinical applications. As summarized in Table 2 and illustrated in Figure 1, fat suppression is useful for improving lesion conspicuity; in expanding the dynamic range of tissue contrast, especially on contrast-enhanced images; in determining whether fat is present or absent in a lesion; in minimizing artifacts from imaging techniques that

Table 2. Common reasons to use fat suppression (and water excitation) versus fat quantification protocols in MRI

Fat suppression and water excitation	Fat quantification
Improve lesion conspicuity Increase tissue contrast dynamic range	Body composition and assessment of adiposity Tissue fat content and characterization • Liver • Pancreas • Heart • Skeletal muscle • Brown adipose tissue • Bone marrow
Establish absence or presence of fat in a lesion	
Minimize image artifacts that arise from fat signals • Chemical-shift artifacts (e.g., DWI EPI) • Subtraction artifacts (e.g., CE-MRA, ASL) • Respiratory motion artifacts	Longitudinal assessment of change in fat content due to therapy and intervention

DWI, diffusion-weighted imaging; EPI, echo-planar imaging; CE-MRA, contrast-enhanced MR angiography; ASL, arterial spin labeling.

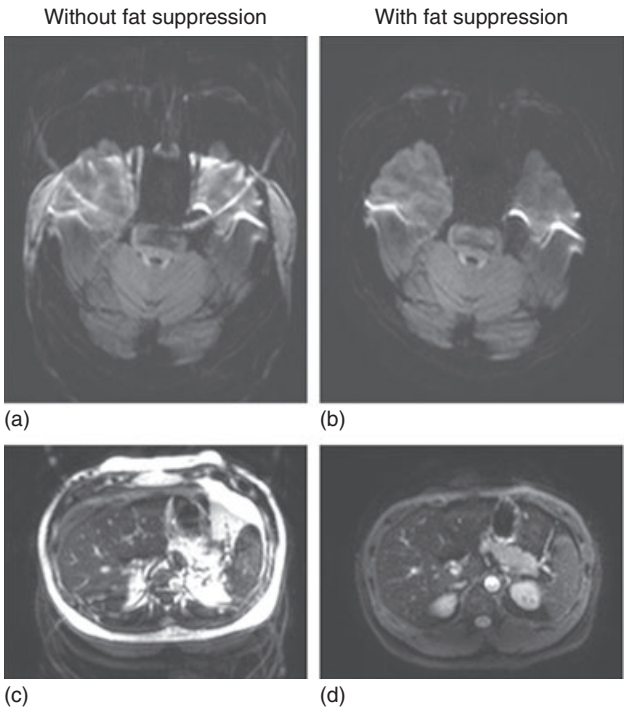

Figure 1. Clinical examples of the utility of CHESS fat-suppression MRI protocols in minimizing chemical-shift artifacts from fat along the phase-encoding direction in (a, b) diffusion-weighted imaging with an echo-planar acquisition and in (c, d) abdominal imaging owing to respiratory motion. All images were acquired on a 3 T Achieva platform from Philips Healthcare. (Courtesy of Jonathan M. Chia, M.S., Philips Healthcare)

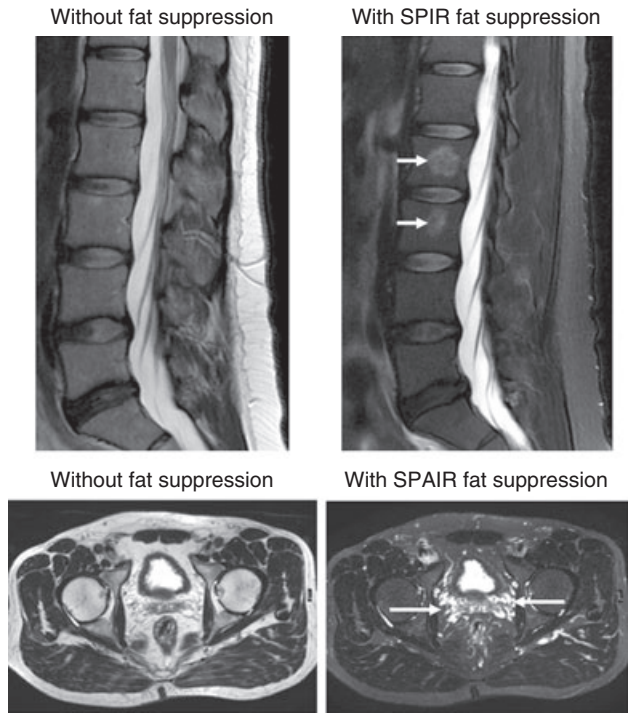

Figure 2. Clinical examples illustrating the utility of CHESS fat suppression. Comparisons are provided against nonfat suppressed counterparts. Pathologies (arrows) in both instances are better visualized with fat suppression, which effectively removes hyperintense signal from fat in bone marrow and adipose tissue. Sagittal images of the spine were acquired on a 3 T Signa platform from GE Healthcare. Axial images of the pelvis were acquired on a 3 T Ingenia platform from Philips Healthcare. (Courtesy of Jeffrey Miller, M.D., and Amber Pokorney, R.T., Phoenix Children's Hospital)

require subtraction of paired images; and in reducing ghosting and spatial distortion artifacts from free-breathing and echo-planar imaging, respectively. Several common strategies for fat-suppression schemes are commercially available.

In one approach, a 180° CHESS RF pulse centered on the methylene fat resonance can be applied to invert the fat magnetization before data acquisition. After an inversion time delay during which the inverted magnetization recovers longitudinally and passes through the zero crossing, the data are acquired and frequency- and phase-encoded such that the signal contribution from methylene fat is minimal. The technique is referred to as SPECIAL (SPECtral Inversion At Lipid) and differs from the conventional T_1-based inversion-recovery approaches (i.e., STIR)[6] in that the inversion pulse for magnetization preparation is fat-selective, and thus, does not affect the water protons. Recent variants of SPECIAL include spectral presaturation with inversion recovery (SPIR) and spectral attenuated inversion recovery (SPAIR). In the former, a fat-selective inversion pulse less than 180° (usually just slightly greater than 90°) is employed, followed by spoiling gradients that dephase the transverse fat magnetization. In the latter, the 180° fat-selective inversion pulse is adiabatic (see ***Adiabatic RF Pulses for MRS***), making the SPAIR approach less sensitive to transverse RF field (B_1) inhomogeneities across large fields-of-view. Figure 2 and Figure 7 illustrate the clinical utility of selective fat suppression in multiple anatomies.

Selective Water Excitation

In lieu of fat suppression, another approach to selectively excite water protons can be achieved with a composite train of binomial RF pulses. The goal of such a series of amplitude-weighted RF pulses (e.g., 1 : 1, 1 : 2 : 1, and 1 : 3 : 3 : 1) is to successively nutate the magnetization of on-resonant water protons into the transverse plane, while the magnetization of off-resonant methylene fat protons is returned to the longitudinal plane, unaffected. This elegant approach, illustrated in Figure 3, is based on setting each of the interpulse delays in the binomial RF pulse train to the time when the water and methylene fat magnetizations are periodically opposed-phase (OP), or equivalently $t_{OP} = 1/(2 \cdot f_F)$, where f_F is the resonant frequency difference between water and methylene fat. Figure 4 illustrates clinical examples of selective water excitation in musculoskeletal applications.

Selective Water Suppression and Fat Excitation

As an alternative to the aforementioned fat suppression and water excitation, complementary fat excitation and water suppression techniques (see ***Water Suppression in Proton MRS of Humans and Animals***) have also been described for specific applications in obesity and metabolism research. The utility of fat-selective excitation has been demonstrated in

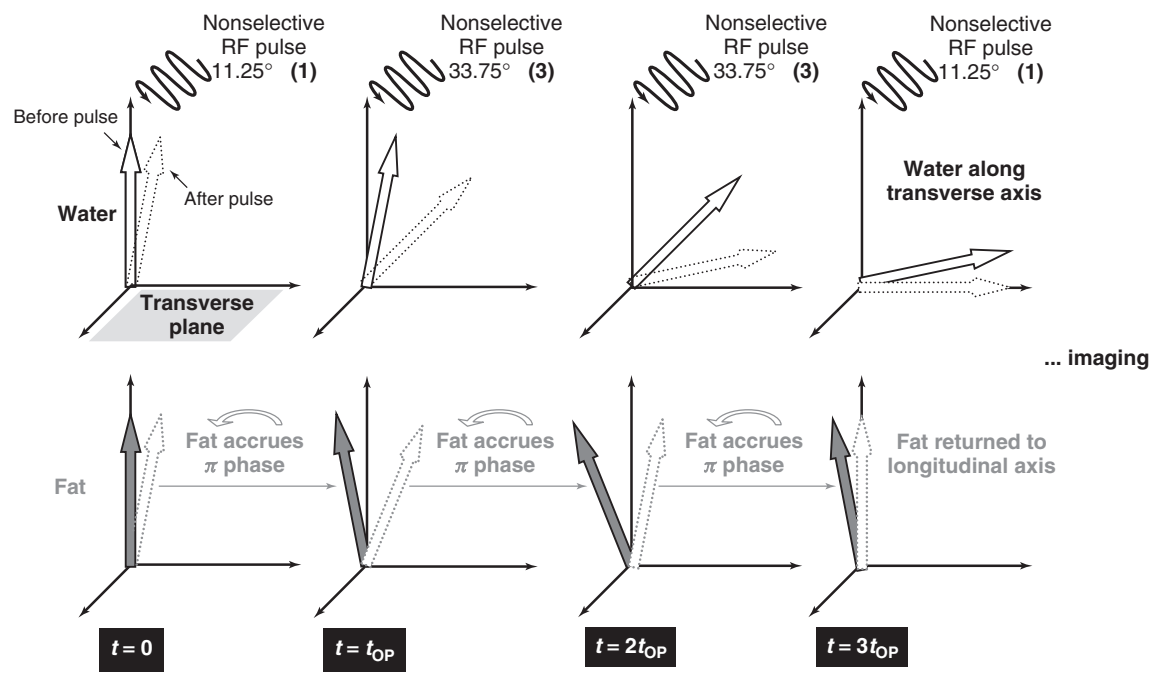

Figure 3. The basic premise of a 1 : 3 : 3 : 1 amplitude-weighted binomial water selective excitation pulse train. The behavior of water and fat magnetizations are shown separately. In each diagram, the magnetization immediately before (solid) and after (dotted) the applied RF pulse are shown. The diagram is shown in the rotating frame centered on the water Larmor resonance. An interpulse period, t_{op}, equal to the time when water and methylene fat magnetizations are oppose-phased, is assumed. Relaxation effects between the RF pulses are negligible and are not shown, for simplicity. While each nonselective pulse constructively adds to the previous one by further nutating the water magnetization into the transverse plane, the fat magnetization experiences a destructive cancellation effect. The net outcome of this RF excitation train is the nutation of the water magnetization by 90° into the transverse plane, while the fat magnetization remains in the longitudinal plane

the quantification of lower extremity, skeletal muscle fat content.[12–14] Conversely, water-suppression techniques that generate fat-only images have been explored as a complementary method to quantify subcutaneous adipose tissue, intra-abdominal and visceral adipose tissue, and intermuscular adipose tissue volumes.[15,16] Water and fat CHESS imaging protocols have also been used in the liver, in conjunction with MRS, to estimate hepatic fat content (see ***In Vivo Hepatic MRS of Humans***), and these methods have been further demonstrated as an effective strategy for comprehensive abdominal fat assessment.[17]

B_0 Inhomogeneity

Main magnetic field (B_0) inhomogeneity, which also causes B_0 off-resonance effects, remains the predominant limitation of CHESS techniques. B_0 inhomogeneity refers to spatially varying deviations of the magnetic field, which can cause unintended resonant frequency drifts on the order of 100–1000 Hz in vivo. Inhomogeneities arise from manufacturing imperfections, perturbations by metallic implants, patient and physiological motion, and from the mere placement of a human body inside the magnet bore. These inhomogeneities are significant around abdominal air-tissue-bowel interfaces, and in the neck and shoulder, the pelvis, the knee, and the ankle anatomies. In the presence of B_0 inhomogeneities, RF pulses designed to selectively suppress fat can erroneously affect water as well. Conversely, an RF pulse intended to target water can inadvertently affect fat. Therefore, magnetic field shimming of the imaging field-of-view is critical in CHESS imaging (Figure 5). As illustrated below, alternative CSE methods provide a means for obtaining more uniform water–fat separation, and thus, fat suppression, in challenging anatomies where CHESS fat-suppression techniques may be inadequate because of large B_0 frequency offsets.

Chemical Shift-Encoded Water–Fat Imaging

The imaging strategies described in the section titled 'Chemical Shift-Selective Imaging' depend on the use of spectrally selective RF pulses to excite or suppress water or fat resonances in order to obtain images depicting only one of these species. An alternative and rapidly emerging approach is CSE water–fat imaging, where images containing both water and fat signals are first obtained by pulse sequences that utilize nonspectrally selective excitation pulses. In CSE MRI techniques, the frequency and resultant phase shifts between water and fat signals are strategically encoded into the acquired data by manipulating the echo-times of the pulse sequence. Subsequently, the water and fat signals are decomposed by mathematical algorithms to yield water-only (i.e., fat-suppressed) and fat-only images, the latter being particularly useful in whole-body assessment of body composition and adiposity (see ***Whole-Body Continuously Moving Table MRI: Principles and Applications***). The

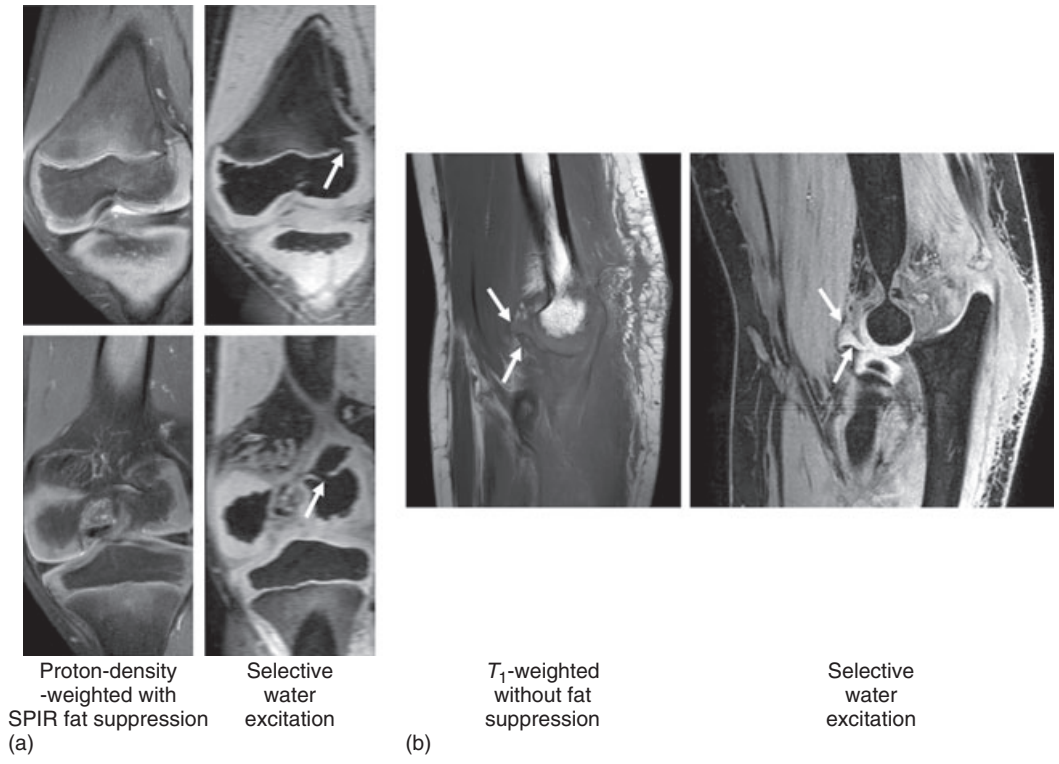

Figure 4. Two examples of CHESS water excitation in musculoskeletal MRI. (a) Two bony bridges (arrows) are observed in this patient's knee, and are better delineated on the selective water excitation images than on conventional proton-density-weighted images with fat suppression. The improved conspicuity in the water excitation images is largely due to the lack of signal in fatty bone marrow. (b) Selective water excitation depicts an osteochondral fracture (arrows) more clearly than T_1-weighted images without fat suppression. All images were acquired on a 3 T Ingenia platform from Philips Healthcare. (Courtesy of Deepa Biyyam, M.D., Craig Barnes, M.D., Scott Jorgensen, M.D., Mittun Patel, M.D., and Amber Pokorney, R.T., Phoenix Children's Hospital)

development of CSE data acquisition techniques and reconstruction algorithms is reviewed in the following sections.[18–20] Table 3 highlights a few of the major methodological advances in CSE water–fat MRI over the past three decades.

Basic Pulse Sequences and Signal Model

CSE acquisitions, typically consisting of multiechoes, or points, can be performed utilizing both spin echo (SE), gradient recalled echo (GRE), and hybrid (SE-GRE) pulse sequences (i.e., GraSE). In SE sequences, the center of the frequency-encoding readout gradient is shifted by a specific duration, t_n, left and right, relative to the center of the Hahn SE. Alternatively, the 180° refocusing RF pulse can be similarly shifted by $t_n/2$ (not t_n) to impart the same net effect. In GRE sequences, images with specific echo shifts can be straightforwardly acquired by setting the appropriate echo times with respect to the center of the excitation RF pulse (Figure 6). These echo-time shifts are needed in order to induce the desired phase differences between water and fat signals, which will enable subsequent water–fat separation algorithms.

Regardless of the acquisition pulse sequence, the collective signal acquired within a single voxel in a CSE imaging experiment can be represented by equation (1).[21] It is assumed that both water and fat magnetizations are present and that the rotating frame of reference is aligned with the Larmor frequency of water. In addition, T_1 and T_2 relaxation effects are ignored for simplicity. Furthermore, a simplified, two-peak water–fat spectral model is again considered at this point.

$$s(t_n) = [s_W \cdot e^{i\phi_W} + s_F \cdot e^{i2\pi f_F t_n} \cdot e^{i\phi_F}] \cdot e^{i2\pi f_B t_n} \quad (n = 1 \ldots N) \tag{1}$$

$$s(t_n) = [s_W + s_F \cdot e^{i2\pi f_F t_n}] \cdot e^{i\phi} \cdot e^{i2\pi f_B t_n} \tag{2}$$

In these equations, s_W and s_F are the intensities of water and fat signals (denoted by subscripts w and f, throughout), respectively; and f_F is the frequency shift of the predominant methylene fat resonance in triglycerides, located approximately 3.4 ppm downfield from the water peak at 37 °C. The frequency shift between water and methylene fat signals is approximately, 217 Hz at 1.5 T and 434 Hz at 3 T. $\phi_{W,F}$ represents the initial phase of the water and fat signals, respectively, and f_B is the frequency offset owing to local B_0-field inhomogeneity. For many GRE and SE pulse sequences, a common initial phase ϕ for water and fat signals can be assumed at the center of the RF excitation pulse ($t = 0$ ms), as shown in equation (2), thereby slightly reducing the number of unknown parameters. The limitations of the simplified spectroscopic model shown in equations (1) and (2) will be discussed in the section

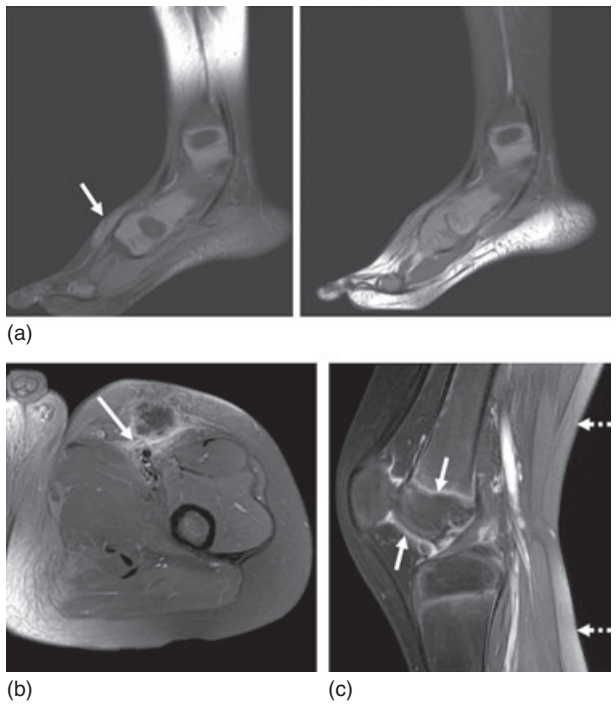

Figure 5. Failure of adequate fat suppression by the SPIR and SPAIR technique owing to B_0 inhomogeneity. In (a), the MR technologist was unable to achieve uniform fat suppression in these ankle T_1-weighted images, after two attempts to shim the imaging field-of-view. Note that, between the two attempts, different regions of the anatomy are fat-suppressed, suggestive of significantly varying B_0 inhomogeneity. The venous malformation on the dorsum of the foot (solid arrow) can be seen in only one of the attempts. In (b) and (c), poor fat suppression can be observed along the perineum and posterior subcutaneous adipose tissue of the knee (dotted arrows), respectively. In these cases, visualization of the abscess and synovial enhancement (solid arrows) are, however, not significantly affected. All images were acquired on a 3 T Ingenia platform from Philips Healthcare. (Courtesy of Deepa Biyyam, M.D., Craig Barnes, M.D., Scott Jorgensen, M.D., Mittun Patel, M.D., and Amber Pokorney, R.T., Phoenix Children's Hospital)

titled 'Quantitative Techniques' in the context of quantitative water–fat imaging.

Equation (2) can be solved using either the natively acquired complex-valued signal $s(t_n)$, or using only the signal magnitude. By removing the phase information, magnitude-based water–fat separation has several inherent advantages, including its insensitivity to phase errors in the acquired source data (e.g., owing to eddy-currents, gradient delays, concomitant gradients, and bipolar readouts), as well as the elimination of phase variations arising from B_0 inhomogeneity.[22] The primary disadvantage of magnitude-based reconstruction techniques is a reduced SNR in the resultant water- and fat-separated images (see also the section titled 'Qualitative Techniques' and Figure 8, below). Furthermore, magnitude-based techniques are able to resolve only a range of 0–50% signal fat fraction, whereas approaches based on complex signals are able to detect a full range of 0–100% signal fat fraction (see the section titled 'Quantitative Techniques').[21]

Table 3. Select methodological developments in CSE water–fat techniques over the past 30 years

Reference	Brief description
Dixon WT, 1984 Sepponen RE, et al. 1984 Blatter DD, et al. 1985	Early conceptual developments and demonstration of CSE feasibility
Glover GH and Schneider E, 1991	Three-echo CSE strategies with B_0 field-map correction
Xiang QS and An L, 1997	Direct CSE phase-encoding strategy
An L and Xiang QS, 2001	CSE with multipeak fat spectrum modeling
Ma J, et al. 2003 Reeder SB, et al. 2005 Doneva M, et al. 2010	Accelerated CSE imaging with: • Parallel imaging • Homodyne reconstruction • Compressed sensing
Ma J, 2004	Two-echo CSE strategy using region-growing and phase-correction concepts
Reeder SB, et al. 2004 Pineda, et al. 2005	Three-echo CSE strategy with asymmetrically sampled echoes and least-squares fitting
Moriguchi H, et al. 2003	Spiral non-Cartesian CSE MRI
Brodsky E, et al. 2008	Non-Cartesian CSE MRI with k-space decomposition
Yu H, et al. 2007 Yu H, et al. 2008	Three + echo CSE strategy with combined B_0 field-map correction, T_2^* estimation, and multipeak fat spectrum modeling
Bydder M, et al. 2011	Multiecho CSE strategy using phase constraints
Eggers H, et al. 2011 Berglund J, et al. 2011	Two-echo CSE strategy with flexible echo times
Berglund J, et al. 2012 Bydder M, et al. 2012 Peterson P, et al. 2013	Multiecho CSE strategies for triglyceride characterization (e.g., chain length, unsaturation degree)

Qualitative Techniques

One of the most utilized aspects of CSE pulse sequences is their ability to provide uniform fat suppression via the water-only reconstructed images, in lieu of traditional CHESS imaging approaches where fat suppression may not be adequate.[23] Figure 7 illustrates comparative examples in multiple anatomies. Using the signal model in equation (2) as a guide, the following section describes CSE strategies that employ acquisitions at one, two, and three or more echo-time shifts.

Single-Echo Methods. Single-echo CSE approaches rely on acquiring an echo when the water and methylene and fat signals are in the real and imaginary channels of the transverse magnetization plane, or are in quadrature ($s(t) = s_W \pm j \cdot s_F$). Specifically, this requires an echo-time shift equal to $(2m+1)/(4 \cdot f_F)$, where m is an integer. The challenge in single-echo approaches is the need to correct for potential differences in the phase of the water and fat magnetizations, as well as B_0 inhomogeneity. These correction factors are typically obtained a priori from a separate calibration scan.[24–26] Although the feasibility of rapid single-echo, water–fat imaging has been demonstrated, its applicability in routine clinical practice has been quite limited.

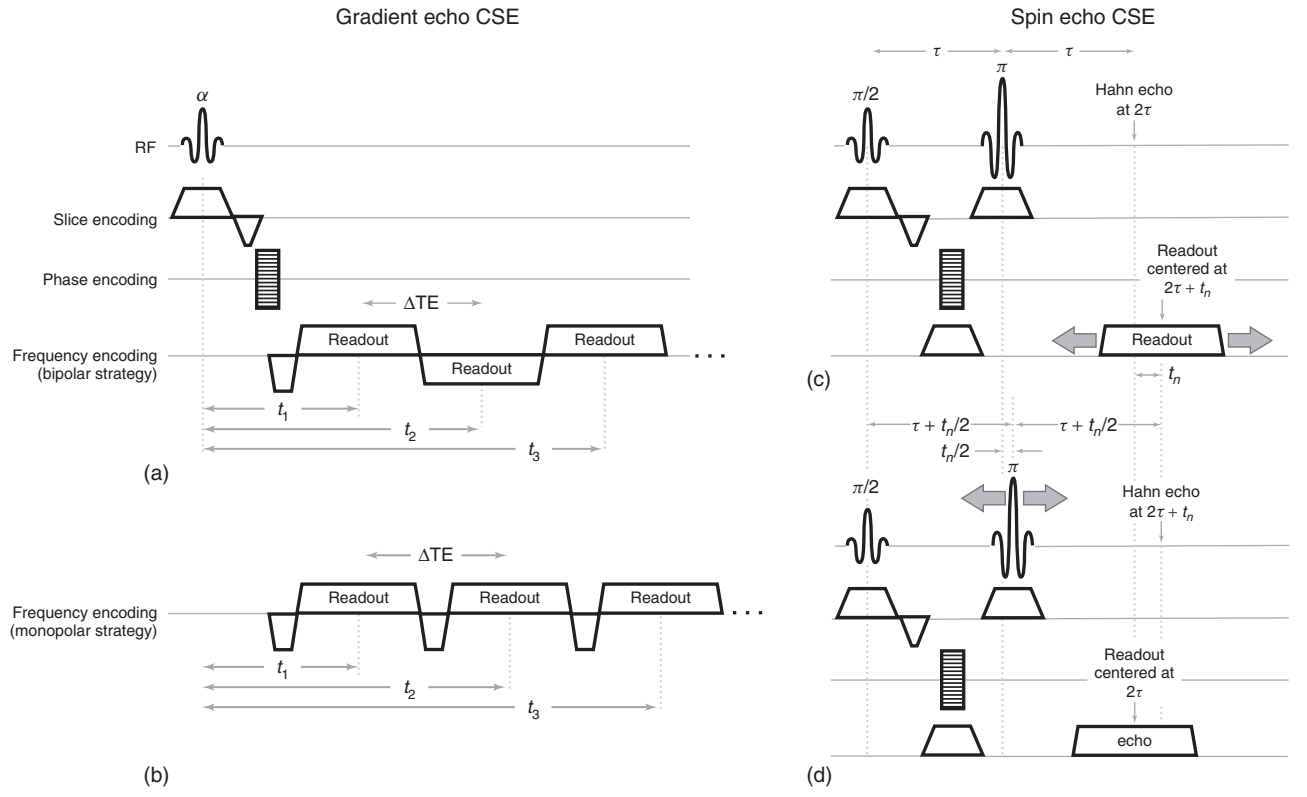

Figure 6. Basic pulse sequence diagrams for (a, b) GRE-based and (c, d) SE-based CSE techniques are shown. In GRE sequences, multiple echoes are typically acquired per TR to encode phase differences between water and fat signals, using either (a) bipolar (nonfly-back) or (b) monopolar (fly-back) readout gradients. The individual time shift, t_n, is equal to the echo time (TE), relative to the center of the excitation RF pulse. Note that with bipolar readout gradients, a shorter echo spacing (ΔTE) between adjacent echoes can be achieved. However, signal polarity and phase errors between odd and even echoes must be accounted for in the reconstruction process. In SE sequences, the desired water–fat phase differences are obtained by (c) shifting the center of the readout gradient, with respect to the center of the Hahn echo. Alternatively as shown in (d), the 180° refocusing RF pulse is shifted by $t_n/2$. With either approach, a shift of t_n between the Hahn echo and the center of the frequency-encoding readout gradient is achieved

Two-Echo Methods. Two-echo CSE strategies are more practical and are frequently utilized in the clinical setting for fat-suppression purposes and to visually detect the presence of fat within an anatomical region of interest (e.g., organ, muscle, and tumor). Historically, the most common two-echo approach is based on a pair of symmetric in-phase (IP) and OP acquisitions, where echo-time shifts, t_n, are judiciously chosen based on the main magnetic field strength, such that signal vectors for water and methylene fat have a phase difference of 0° ($s(t_{IP}) = s_W + s_F$) and 180° ($s(t_{OP}) = s_W - s_F$), respectively. Intuitively, it is apparent that if both water and fat are present within a voxel, the net magnitude of the OP signal will be smaller than that of the IP signal. In recent years, emerging and robust two-point strategies that do not require strict adherence to the symmetrical acquisition of IP and OP echoes have been proposed.[27–29]

On the basis of equation (2), a two-point strategy that acquires two complex-valued signals, $s(t_n)$, can enable estimation of the four unknowns, s_W and s_F, their common phase ϕ, and B_0 inhomogeneity f_B. The fundamental challenge in two-point, water–fat separation algorithms is to correctly account for the time-dependent phase shifts introduced by f_B. Artifacts known as water–fat swaps, or signal ambiguities, can arise in equation (2) in voxels that contain only water or fat. Therefore, the signal generated from a water voxel, with s_W having an amplitude of A that is experiencing an f_B of, for example, x Hz, will be indistinguishable from a pure fat voxel having the same amplitude A and experiencing an f_B of $x \pm f_F$ Hz. A majority of water–fat separation algorithms exploit the fact that f_B is not independent from voxel to voxel, but is rather spatially smooth. This assumption is frequently used to initialize the estimation of f_B at a particular voxel, based on *a priori* estimated f_B values at adjacent seed or neighboring voxels. Phase-unwrapping techniques have also been introduced to mitigate the water–fat signal ambiguity problem.[30,31]

Three or More Echo Methods. The use of additional echoes beyond the traditional two-point approach in CSE water–fat separation enables a closed form solution for f_B in equation (2).[32,33] As a simple example, if two echoes are separated by one or more complete ($\pm 2\pi$) cycles of the methylene fat signal about the water signal, then the water and fat signals in these two echoes will possess the same relative phase difference. Any additional nonzero phase accrual between the two points can be attributed to f_B. Once f_B is determined, its effect can be demodulated from all of the

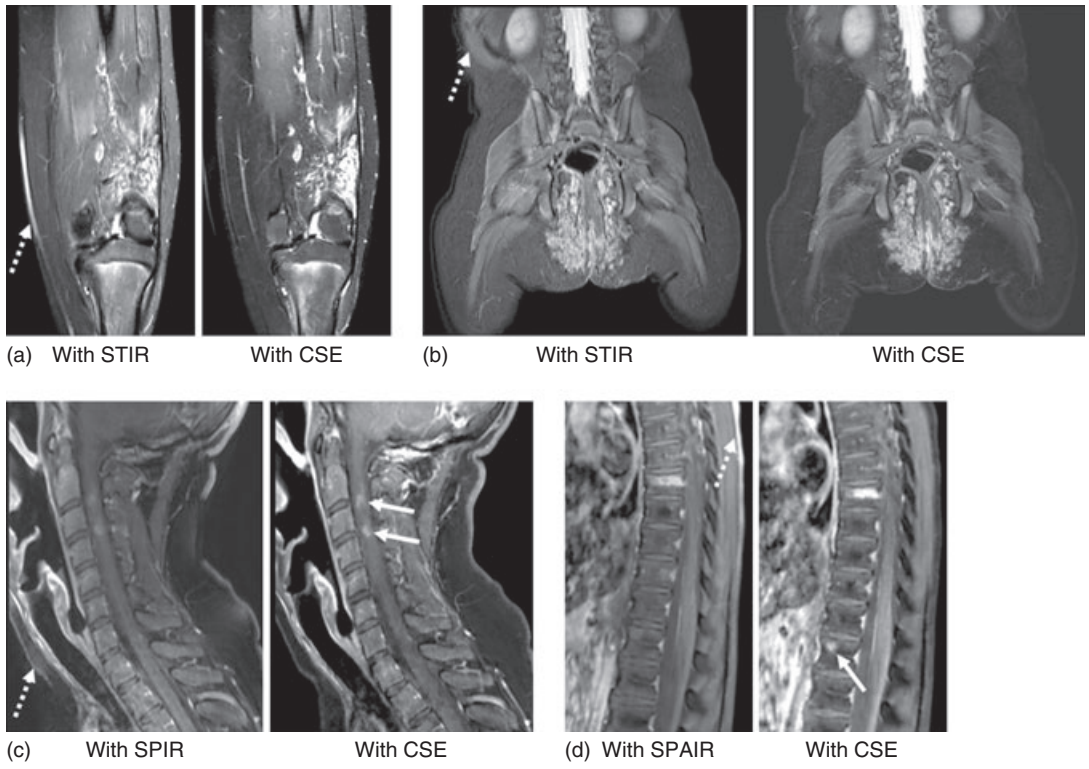

Figure 7. Clinical examples of the utility of CSE fat-suppression MRI protocols in improving lesion conspicuity. Comparisons are made between CSE water-only reconstructed images and other fat-suppression techniques. In (a) and (b), improved lesion conspicuity of the vascular malformation and hemangioma is observed with reconstructed water-only images from CSE MRI than with traditional T_1-based short-TI inversion recovery (STIR) techniques, respectively. In (b), superior fat suppression with CSE is evident. In (c) and (d), lesions within the spinal cord and vertebral bone marrow are significantly better visualized with CSE MRI (solid arrows). Dotted arrows point to regions of fat-suppression failure. All images were acquired on a 3 T Ingenia platform from Philips Healthcare. (Courtesy of Smita Bailey, M.D., Deepa Biyyam, M.D., Craig Barnes, M.D., Patricia Cornejo, M.D., Scott Jorgensen, M.D., Mittun Patel, M.D., Jeffrey Miller, M.D., and Amber Pokorney, R.T., Phoenix Children's Hospital)

acquired echoes, leaving s_W and s_F, and the phase ϕ, as the unknowns to be solved.

The robust and explicit estimation of f_B remains a key challenge in CSE water–fat imaging. Multiple algorithms have been developed over the past decade to address the effects of an inhomogeneous B_0 field. Table 4 lists several major efforts toward f_B estimation, grouped by methodology. Fundamentally, a large majority of current techniques continue to share the common notion that f_B is spatially smooth across localized regions in vivo. Spatial region-growing schemes, which expand from the initial seed voxels where reliable f_B values are first obtained, are popular. Hierarchical and multiple resolution algorithms that first estimate f_B at a coarse resolution and subsequently proceed to finer resolution stages using iterative propagation are practical options. Regularized formulations that use a cost function to determine a water–fat separation that fits the acquired source data and satisfies the constraint of a spatially smooth-varying B_0-field map also have desirable properties for estimating f_B. In particular, regularized techniques enable the introduction of explicit a priori knowledge that facilitates characterization of the estimates (e.g., degree of smoothness of the estimated f_B map). Further, regularized techniques often lead to minimization problems that are solvable using more generalized and powerful algorithms (e.g., graph cuts). In addition, novel and emerging strategies that do not require the smoothness assumption show promise: these use alternative estimates, such as the local magnetic susceptibility, to initialize and complement the f_B estimation process. The importance of estimating B_0 inhomogeneity in the context of CSE water–fat imaging was underscored in the 2012 competition organized by the ISMRM (http://www.ismrm.org/challenge/), where several investigator teams competed to develop the most robust algorithm.

The use of three or more echo points affords the user more flexible choices in echo times, with the potential to achieve shorter interecho spacings with more robust estimation of f_B across a greater off-resonance range. As the nominal chemical-shift frequency difference between water and methylene fat is doubled at 3.0 T compared to 1.5 T, more closely spaced echo-time shifts are needed at 3.0 T and at higher B_0 field strengths to achieve the same relative water–fat phase difference. Depending on the anatomy to be imaged and other tradeoffs between scanner settings and the desired acquisition time (e.g., within a breath-hold, gradient strengths), the requisite echo-time shifts, t_n, and interecho spacings, ΔTE (see below), may be achieved by a combination of monopolar or bipolar readout gradient schemes (Figure 6), and by acquiring all echoes within a single TR of the acquisition pulse sequence (i.e., echo train length $= N$) or in an interleaved multishot manner.

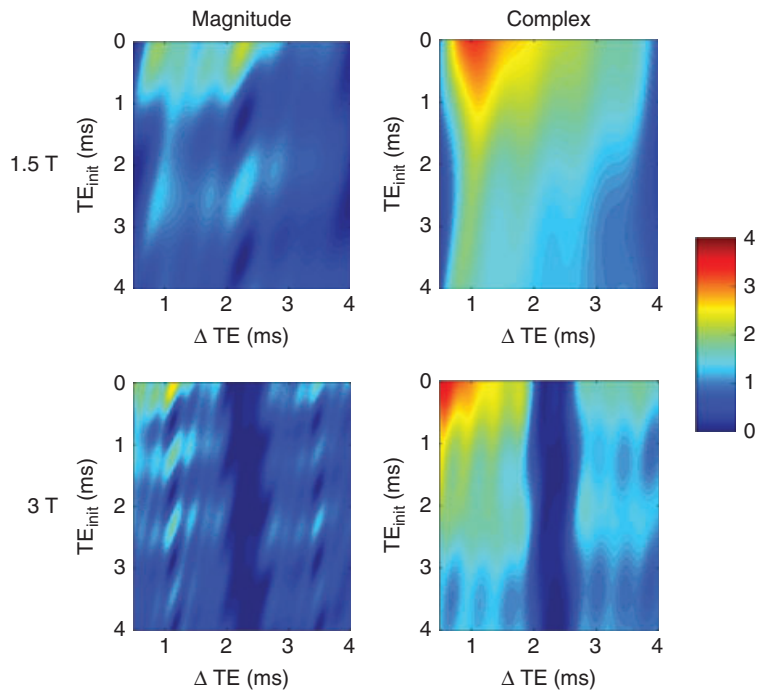

Figure 8. Simulated NSA (effective number of signal averages, color-scale at right) maps for the fat component using magnitude and complex fitting at 1.5 and 3 T, which are useful in guiding the design of an SNR-optimized CSE pulse sequence. The maps are shown as a function of the interecho spacing (ΔTE) and the first (shortest achievable) echo-time shift, TE_{init}. Note that complex fitting typically yields higher NSA values than magnitude fitting, and that the latter has multiple 'dark blue' areas of low NSA. Furthermore, short interecho spacings and short initial echo times generally yield the highest NSA values. In the 3 T plots (bottom row), note the 'valley' of low NSA values for an interecho spacing around 2.3 ms. This corresponds to a phase accrual that is nearly equal to 2π between each successive echo. Other simulation parameters include: six echoes; a single $R_2{}^*$ signal model with $R_2{}^* = 40\ s^{-1}$; a voxel containing $s_w{:}s_f = 9:1$ (e.g., a signal fat fraction of 10%); and a six-peak spectral model of fat

Table 4. Select methodological developments in the estimation of a B_0 inhomogeneity field-map in multiecho CSE water–fat imaging over the past decade

Reference	Type of approach
Yu H, et al. 2005	Region-growing techniques
Berglund J, et al. 2010	
Lu W and Hargreaves BA, 2008	Multiresolution techniques
Sharma SD, et al. 2012	
Tsao J and Jiang Y, 2013	
Hernando D, et al. 2008	Linear prediction techniques
Jacob M and Sutton BP, 2009	
Hernando D, et al. 2010	Joint estimation and regularization techniques
Soliman AS, et al. 2014	
Cui C, et al. 2014	
Sharma SD, et al. 2014	Hybrid and alternative techniques
Liu J and Drangova M, 2014	

For three-point CSE acquisitions particularly, the SNR-optimized echo-time shifts and interecho spacings have been derived using the Cramér–Rao formalism.[34] Not surprisingly, the SNR-optimal ΔTE for a three-point CSE acquisition was found to correspond to a relative phase-shift of $2\pi/3$ between water and methylene fat signals. Furthermore, asymmetric echo sampling (e.g., non-IP and non-OP) exhibited superior SNR characteristics compared to traditional symmetric sampling schemes. To quantitatively compare the performance of various multiecho CSE acquisitions, a useful metric, the effective number of signal averages (NSA), has been introduced. NSA is mathematically defined as the ratio of the noise variance in a source t_n image to the noise variance in the separately reconstructed water or fat images. Conceptually, the NSA metric characterizes how noise propagates from the acquired source images to the resultant water-only and fat-only decomposed images: it has been shown that the maximum achievable NSA is equal to the number of acquired source echoes, N. The NSA metric aids in the design of imaging protocols by enabling the prediction of the performance of a CSE acquisition and the quality of the subsequent water–fat separation results. The NSA behavior and the design of an SNR-optimized CSE protocol are significantly influenced by the proper selection of the initial echo time, t_1; the interecho spacing, ΔTE; the inclusion of inhomogeneously broadened transverse ($T_2{}^*$) relaxation effects (see below); the use of multipeak water–fat spectral models (see the section titled 'Single versus Multipeak Fat Spectrum') of the signal; the degree of B_0 field inhomogeneity; the target signal fat-fraction range (i.e., the ratio of s_W to s_F); as well as the utilization of magnitude versus complex reconstruction algorithms (Figure 8).

Most numerical algorithms for multiecho water–fat separation can be classified into one of two groups. The first group of approaches consists of analytical algorithms, where a closed-form solution for the unknown parameters is provided

using a subset or all of the acquired echo-time shifts. Some of these methods aim to first provide an analytical solution for the B_0 inhomogeneity term, f_B. Upon the estimation of an f_B map, its effect is demodulated from the acquired signals, $s(t_n)$, and s_W and s_F are subsequently estimated (e.g., using linear least-squares fitting). The second group of algorithms estimates *all* of the unknown parameters directly by posing the estimation as a nonlinear least-squares fitting problem (i.e., using the maximum-likelihood criterion in the presence of Gaussian noise). Nonlinear least-squares methods provide good SNR performance and flexibility in the formulation of the most plausible solution, especially when they are combined with regularization. However, nonlinear least-squares methods are typically characterized by increased computational complexity, owing to the need for an iterative algorithm to reach a solution.

Multiecho CSE strategies can further facilitate the introduction of additional parameters into the signal model for estimation. With the acquisition of three complex-valued signals $s(t_n)$, two more unknowns in addition to s_W, s_F, ϕ, and, f_B can be considered. One highly relevant parameter is T_2^* ($1/R_2^*$) relaxation, which characterizes the rate of signal decay between multiple echoes. Equations (3) and (4) illustrate the updated signal model from equation (2), with separate R_2^* terms for water and fat or a common water–fat R_2^* term, respectively.[35] Model variants that assume separate initial phases for water and fat are often used as well.

$$s(t_n) = [s_W \cdot e^{-R_2 *_W \cdot t_n} + s_F \cdot e^{i2\pi f_F t_n} e^{-R_2 *_F \cdot t_n}] \cdot e^{i\phi} \cdot e^{i2\pi f_B t_n} \quad (3)$$

$$s(t_n) = [s_W + s_F \cdot e^{i2\pi f_F t_n}] \cdot e^{i\phi} \cdot e^{i2\pi f_B t_n} \cdot e^{-R_2 * \cdot t_n} \quad (4)$$

The inclusion of T_2^* into the signal model leads to more accurate water–fat separation and estimates of s_W and s_F. However, it is accompanied by lower relative NSA performance, compared to models that exclude T_2^*. For this reason, T_2^* estimation is generally considered unnecessary for fat-suppression applications that are qualitative. However, for quantitative applications (see the section titled 'Quantitative Techniques'), correction for T_2^* effects is required in order to achieve highly accurate and precise estimates of ectopic and organ fat content.[36]

Quantitative Techniques

In this section, we summarize the recent development of CSE strategies for quantitative fat imaging (Table 2).[37] Emphasis is specifically placed on significant advances in the establishment of an accurate, precise, and reproducible quantitative imaging biomarker of tissue fat, known as the *proton-density fat fraction* (PDFF).[38] The use of quantitative CSE imaging and the PDFF biomarker has risen steadily in recent years, and its clinical utility in assessing ectopic tissue fat concentrations in vivo is emerging, particularly in liver and skeletal muscle. Indeed, PDFF CSE imaging has been widely adopted in recent studies of obesity and metabolic disorders. The accumulation of fat in subcutaneous and visceral white adipose tissue compartments, in conjunction with the deposition of fat in the liver (see ***Monitoring Fatty Liver***), heart (see ***Cardiac Lipids by ^1H MRS***), and skeletal muscle (see ***Muscle studies by ^1H MRS***), are recognized determinants of metabolic health risks (see ***Insulin resistance, type 2 diabetes and obesity and other metabolic disorders studied by MRS***, ***In Vivo MRS of Lipids in Adipose Tissue, Bone Marrow, and Liver***, ***Body Fat MRS***). Accurate, precise, and objective quantitative fat measurements can assist physicians with diagnosis, health risk assessment, and disease stratification in conditions such as nonalcoholic fatty liver disease (Figure 9), neuromuscular disorders (Figure 10), bone marrow diseases, and type II diabetes. These measurements can facilitate cross-sectional studies that compare subcutaneous and visceral adipose tissue distributions between various groups (e.g., age, gender, and ethnicity). Similarly, longitudinal measurements can determine the efficacy of therapies and interventions designed to alter body and organ fat levels, and capture temporal changes in fat accumulation.

As alluded to in the sections titled 'Basic Pulse Sequences and Signal Model' and 'Qualitative Techniques', although qualitative CSE water–fat imaging can be performed using a wide variety of GRE and SE pulse sequences, quantitative PDFF CSE imaging has been confined to spoiled gradient echo sequences in the literature. The primary reason for using a spoiled gradient echo sequence is its relatively simple approach to achieve proton-density-weighted signal contrast, through the use of small RF excitation flip angles and short TR. Quantitative PDFF CSE protocols are typically performed with at least three echoes. The use of six or more echoes is common in current clinical practice and research studies, and is largely driven by the need to ensure numerical stability and sufficient SNR in estimating T_2^* and f_B, while performing water–fat separation. At 1.5 T, the requisite echo times are often acquired using monopolar (i.e. fly-back) readout gradients and a single echo train of length N per TR, with the spacing between consecutive echoes (ΔTE) set between 2 and 3 ms (Figure 6). At 3.0 T, multiple interleaved echo trains with monopolar readout gradients are typically required to achieve a shorter ΔTE of 1–1.5 ms. Alternatively, echo trains with bipolar (i.e. nonfly-back) readout gradients can be employed, at the expense of additional postprocessing steps. These steps are needed to properly align and correct for phase errors in the echoes from opposite-polarity readout gradients.[39]

At this point, it is important to draw a distinction between the definitions of signal fat-fraction and PDFF. For any CSE water–fat imaging techniques, it is straightforward to calculate a voxel-wise signal fat fraction after water–fat separation, defined as $FF = s_F / (s_W + s_F)$ for each voxel (see the section titled 'Noise Considerations'). However, this particular FF carries no significant clinical meaning and is highly pulse sequence- and MR scanner platform-dependent, as the s_W and s_F amplitudes depend on the specific signal contrast weighting of the acquisition pulse sequence (e.g., RF excitation flip angle, TR, and TE). Furthermore, s_W and s_F are individually influenced by their respective proton densities and relaxation parameters (e.g., T_1, T_2, and T_2^*). In contrast, the PDFF measures the ratio of MR-visible protons arising from fat to all MR-visible protons arising from both fat and water. It is a ratio of fat and water proton densities only, excluding the effects of relaxation and other physiological signal confounders. Therefore, in order to compute PDFF, these confounders need to be addressed by a

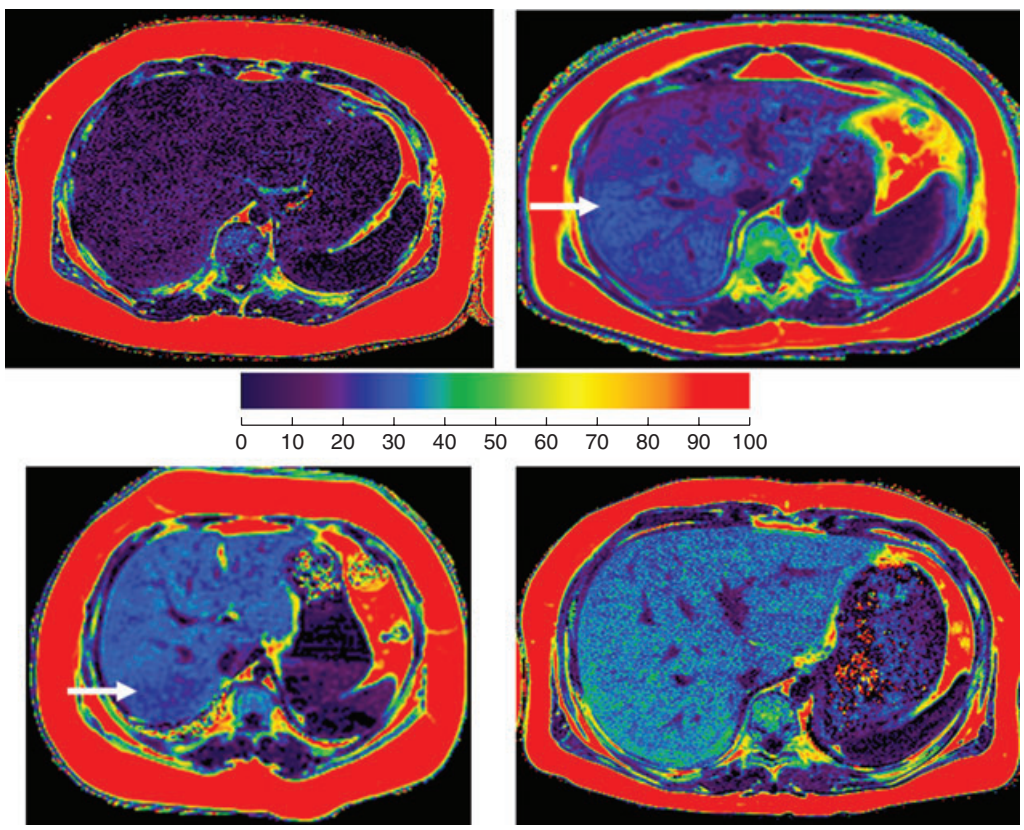

Figure 9. Examples of quantitative CSE in the liver using a six-echo acquisition protocol and T_2*-corrected data reconstruction. PDFF maps (color scale 0–100%) from four Hispanic adolescents are shown, demonstrating progressively increasing fat content. Note the appearance of heterogeneous fat infiltration in two subjects (arrow). All images were acquired on a 3 T Signa platform from GE Healthcare

combination of data acquisition and reconstruction processes. These techniques are summarized next, in the context of a spoiled gradient echo pulse sequence.

T_2 Relaxation.* In multiecho CSE acquisitions, transverse relaxation inevitably introduces signal decay as echo time increases. Furthermore, T_2* values can be quite short (<5 ms) in organs such as the liver and the heart in patients with iron overload. If not corrected, the presence of T_2* decay results in bias and poor accuracy and precision in PDFF quantification. As previously shown in equation (4), T_2* decay can be included in the CSE signal model, and its effects can be corrected in water–fat reconstructions by effectively extrapolating the water and fat signals to $t = 0$ ms. While the inclusion of an additional unknown parameter into the signal model consequently results in a reduction in SNR, multiple investigators have shown that correcting for T_2* decay is critical for accurate PDFF quantification.[40,41] The use of a common T_2* value for water and fat signals ($T_2{}^*_W = T_2{}^*_F$) has been shown to be a practical tradeoff between PDFF accuracy and the resultant NSA of water- and fat-separated images. This model is sufficiently accurate in many clinical applications and is simpler to solve than the dual T_2* approach of equation (3).

T_1 Recovery. It is well known that fat protons have a significantly shorter T_1 relaxation time compared to tissue water signals in vivo. This two- to threefold difference in T_1 values can introduce differential T_1 weighting to the acquired water, s_w, and fat, s_f, signals. If not minimized or corrected, the resultant signal fat fraction will exhibit a preferential T_1 bias toward the shorter-T_1 fat signal, often resulting in overestimation of the underlying PDFF.[42,43] In current clinical practice, a majority of quantitative CSE strategies use low RF excitation flip angles–on the order of 10°–15° in 2-D (two-dimensional) imaging and 3°–5° in 3-D imaging–to minimize T_1 bias in PDFF computations. Despite some penalties in SNR, this low-flip-angle approach has been shown to enable accurate PDFF CSE imaging in clinical applications, thus removing the need to explicitly perform T_1 mapping and signal correction.

Single vs Multipeak Fat Spectrum. For the purpose of achieving an accurate quantitative PDFF endpoint, it seems appropriate that a more realistic representation of the triglyceride spectrum is used in lieu of the single-peak methylene-only adaptation. It is estimated that the methylene resonance reflects only approximately 70% of the total multipeak triglyceride signal, and therefore, will underestimate PDFF. In theory, although the signal model can be expanded to include multiple s_F unknowns – one for each of the triglyceride proton resonances – this approach is often numerically impractical because of the poor spectral resolution of CSE acquisitions.[44] In practice, a predetermined multipeak spectrum is used, where the relative chemical-shift frequency offsets (with respect to

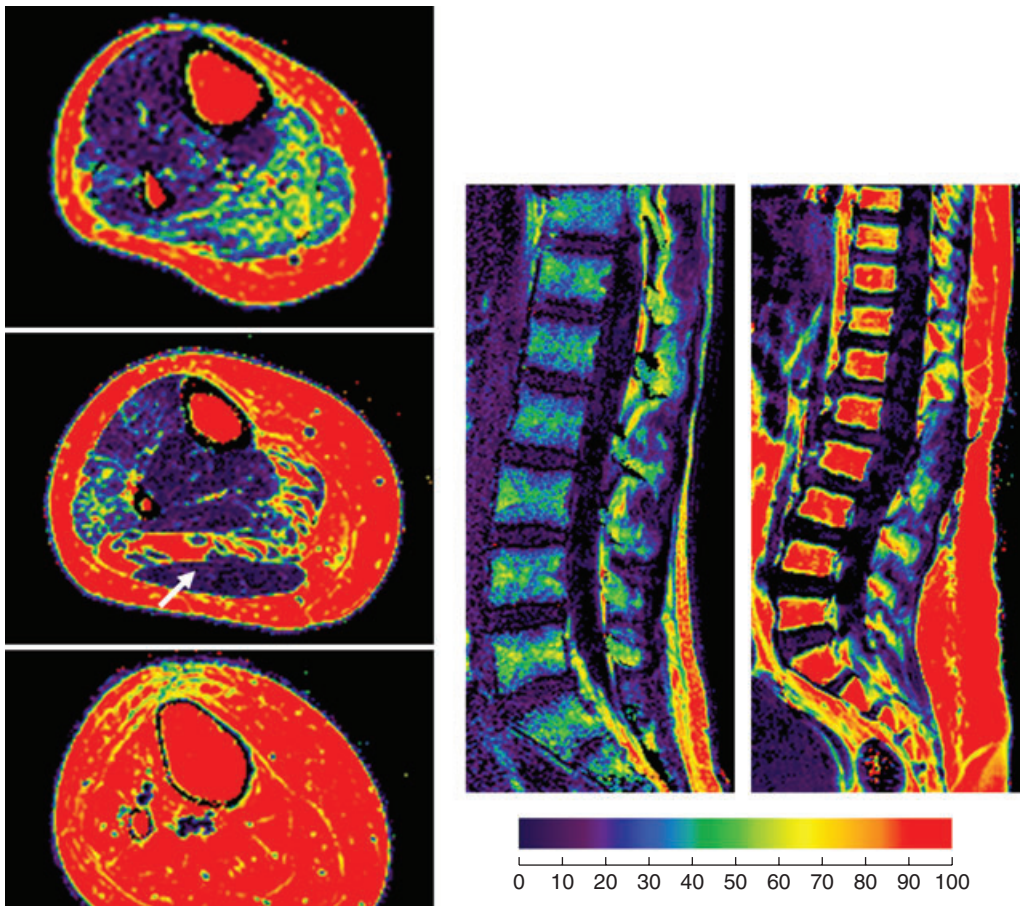

Figure 10. Examples of quantitative CSE in the (a) lower extremity musculoskeletal system and in (b) vertebral bone marrow using a six-echo acquisition protocol and T_2^*-corrected data reconstruction. (a) PDFF maps from three spina bifida patients are shown (color scale 0–100%). Various degrees of fat accumulation can be seen, including preferential fat accumulation in the soleus and gastrocnemius medial muscles (middle), while the gastrocnemius lateral muscle is unaffected (arrow). By comparison, all three muscles are affected, but to a lesser extent, in the top subject. In the bottom subject, complete replacement of skeletal muscles by fat is evident. (b) PDFF maps from a 15-year-old healthy control (left) and an 11-year-old patient (right) are shown. Note the high fat fractions of the vertebral bone marrow in the patient, owing to the reduction of hematopoietic red bone marrow as a consequence of radiation therapy, for treatment of a malignant giant cell tumor. All images were acquired on a 3 T Achieva platform from Philips Healthcare. (Courtesy of Skorn Ponrartana, M.D., Nicole Mueske, M.S., and Tishya Wren, Ph.D., Children's Hospital Los Angeles)

water) and the amplitudes of each triglyceride resonance are assumed to be known and measured a priori.[45] Extensive efforts in recent years have been devoted to accurately characterizing the multipeak fat spectrum in humans in vivo.[46,47]

By adopting this precalibrated multipeak approach, the signal model from equation (4) can be expanded and rewritten as shown in equation (5), without introducing any additional unknown parameters:

$$s(t_n) = \left[s_W + s_F \cdot \sum_{p=1}^{P} a_p e^{i2\pi f_{F,p} t_n} \right] \cdot e^{i\phi} \cdot e^{i2\pi f_B t_n} \cdot e^{-R_2 * \cdot t_n} \quad (5)$$

Here, the fat spectrum is modeled by P resonance peaks with relative amplitudes, a_p, such that the sum of these amplitudes equals 1. For, each peak, p, $f_{F,p}$ represents its resonant frequency difference relative to water. Note that equation (5) assumes a common T_2^* value for water and all P peaks of the fat spectrum. Equation (3) can be similarly expanded to include the P peaks, with individual T_2^* terms assigned to water and each of the P fat resonances. Throughout the literature, several variations of multipeak fat spectral models have been proposed and utilized. While it has been suggested that the triglyceride spectrum varies slightly with respect to the degree of unsaturation in humans in vivo, such subtle physiological variations are unlikely to have a major impact on the accuracy of the resultant PDFF. Indeed, a recent work has shown that the choice of a particular multipeak model has negligible effects on the accuracy of PDFF.[48]

Phase Errors. In multipoint CSE imaging with a spoiled gradient echo pulse sequence, phase errors can often arise between the echoes owing to eddy current effects, delays in the gradient hardware, concomitant gradients, and bipolar gradient readout

schemes.[49] A simple approach to address these phase errors is to completely discard the phase component from the source data and perform a magnitude-based reconstruction. This strategy is represented by equation (6), where previous terms describing the effects of initial phase ϕ and B_0 inhomogeneity have been eliminated:

$$|s(t_n)| = \left| s_W + s_F \cdot \sum_{p=1}^{P} a_p e^{i2\pi f_{F,p} t_n} \right| \cdot e^{-R_2 * \cdot t_n} \quad (6)$$

Alternative hybrid magnitude- and complex-based approaches have been proposed, as well as strategies that explicitly model and solve the phase errors with additional terms.[39]

Temperature. It is well known from NMR-based thermometry that temperature influences the proton resonant frequency of tissue water, at a rate of approximately −0.01 ppm per degree Celsius. While the discussion up to this point has used notations in the equations assuming a triglyceride spectrum that is relative to the water resonance at a physiological temperature of 37 °C for humans, a correction factor must be applied to the $f_{F,p}$ terms in phantom experiments, which are usually carried out at room temperature, in preclinical animal experiments that use heating pads during MRI data acquisition, and in postmortem experiments. The effects of temperature on the accuracy and reproducibility of PDFF estimates have recently been demonstrated.[50]

Noise Considerations. After accounting for the aforementioned confounders, the separated water and fat signals, s_W, and s_F, accurately reflect the true proton densities of water and fat. While it may appear logical and intuitive at this point to compute the PDFF, as suggested below in equation (7) by taking the magnitude of the signals, such an approach would introduce additional bias into the estimation, particularly at low and high fat-fractions, owing to the rectification of noise in the $|s_W|$ and $|s_F|$ operations. To eliminate this noise bias, alternative formulations have been proposed for low (0–10%) and high (90–100%) fat fractions, as outlined in equations (8) and (9), respectively:[42]

$$\text{PDFF} = \frac{|s_F|}{|s_F| + |s_W|} \quad (7)$$

$$\text{PDFF} = 1 - \frac{|s_W|}{|s_F + s_W|} \quad (8)$$

$$\text{PDFF} = \frac{|s_F|}{|s_F + s_W|} \quad (9)$$

Future Directions

Quantitative CSE imaging is a rapidly growing field, with important methodological advances in recent years. In addition to estimating the traditional water, fat, B_0-field map, and T_2^* relaxation parameters, extended signal models have been proposed to further approximate triglyceride properties, such as chain length and mono- and polyunsaturation levels.[51,52] In the aforementioned signal models, the amplitude term, α_p, is further expanded using theoretical equations that directly relate the number of protons to triglyceride chain length and the number of double bonds. For example, each triglyceride model has a constant of nine protons for the ($-CH_3$) resonance; the total number of protons along the glycerol backbone is always 17; the number of olefinic protons ($-C\underline{H}=C\underline{H}-$) is always equal to twice the number of double bonds; and the number of diacyl protons ($-CH=CH-C\underline{H}_2-CH=CH-$) is always equal to twice the number of methylene-interrupted double bonds.[47] However, the research potential and clinical utility of such expanded signal models has been limited, owing to the requirement that a large number of echoes (e.g., 16–32) must be acquired, leading to long scan times.

Another area of continued interest is the development of rapid and efficient non-Cartesian *k*-space sampling trajectories in conjunction with CSE pulse sequences. Some common advantages of non-Cartesian sampling schemes are (i) their tendency to oversample the center of *k*-space, thus facilitating self-navigated motion correction and (ii) their ability to sample the center of *k*-space with a very short echo time, which enables incorporation of additional ultrashort T_2 species (e.g., cortical bone, tendons, ligaments, and menisci) into the water component of the signal model. While the feasibility of non-Cartesian CSE imaging has been shown with a variety of spiral and radial *k*-space trajectories, these techniques have so far not been widely adopted in routine clinical applications for fat suppression and fat quantification. Finally, the feasibility of applying the CSE formalism to other proton-based chemical species, such as silicone, as well as nonproton nuclei, such as Carbon-13, has been demonstrated. As these technical developments continue to emerge, their translation into clinical applications will undoubtedly be explored.

Conclusion

In conclusion, CHESS and CSE strategies for direct water–fat proton imaging have become an indispensable asset in research and clinical MRI applications. Compared to MRS and CSI, the fundamental underpinnings of these techniques highlight the relative mathematical simplicity of adopting a predefined water and fat spectrum a priori. Direct imaging approaches provide intuitive solutions with high spatial resolution, albeit at the expense of low spectral resolution. This article has attempted to provide the reader with sufficient introductory materials and literature references on the topic, from traditional fat suppression endpoints to more recent efforts in quantitative fat applications.

Acknowledgments

H. Hu acknowledges the funding support from Philips Healthcare and reference assistance from librarian Kathy Zeblisky at Phoenix Children's Hospital. D. Hernando acknowledges the support from GE Healthcare.

Biographical Sketches

Houchun Harry Hu. b 1979. BSc, 2001, PhD, 2006, Mayo Clinic. Has performed research in parallel imaging, continuously moving

table MRI, angiography, and water–fat MRI. Postgraduate training at the University of Southern California and Children's Hospital Los Angeles. 2012 to present, served as Deputy Editor of Magnetic Resonance in Medicine. Approximately 60 published papers in MRI. Current research interests: pediatric imaging, childhood obesity.

Diego Hernando. b 1978. BSc, 2002, PhD, 2010, University of Illinois at Urbana–Champaign. Has performed research in experiment design, image reconstruction, and parameter estimation in the context of MRI. Since joining the Department of Radiology at the University of Wisconsin–Madison in 2010, his main research focus has been the development and translational validation of quantitative imaging biomarkers, with an emphasis on fat and iron quantification. Dr. Hernando has published approximately 40 papers on MRI.

Related Articles

Body Fat Metabolism: Observation by MR Imaging and Spectroscopy; In Vivo Hepatic MRS of Humans; Selective Excitation in MRI and MR Spectroscopy; Tissue Water and Lipids: Chemical Shift Imaging and Other Methods; Water Suppression in Proton MRS of Humans and Animals; Ultrafast Multidimensional NMR: Principles and Practice of Single-Scan Methods; Whole-Body Continuously Moving Table MRI: Principles and Applications; Muscle studies by ^{1}H MRS; In Vivo MRS of Lipids in Adipose Tissue, Bone Marrow, and Liver; Adiabatic RF Pulses for MRS; Cardiac Lipids by ^{1}H MRS; CSI and SENSE CSI; 2D MRS; Insulin resistance, type 2 diabetes and obesity and other metabolic disorders studied by MRS; Monitoring Fatty Liver; Body Fat MRS

References

1. H. H. Hu, P. Börnert, D. Hernando, P. Kellman, J. Ma, S. B. Reeder, and C. B. Sirlin, *Magn. Reson. Med.*, 2012, **68**, 378.
2. E.de Kerviler, A. Leroy-Willig, O. Clément, and J. Frija, *Biomed. Pharmacother.*, 1998, **52**, 69.
3. E. M. Delfaut, J. Beltran, G. Johnson, J. Rousseau, X. Marchandise, and A. Cotton, *Radiographics*, 1999, **19**, 373.
4. S. S. Pokharel, K. J. Macura, I. R. Kamel, and A. Zaheer, *Radiographics*, 2013, **33**, 681.
5. J. W. Rampton, P. M. Young, J. L. Fidler, R. P. Hartman, and R. J. Herfkens, *Am. J. Roentgenol.*, 2013, **201**, 1303.
6. G. M. Bydder and I. R. Young, *J. Comp. Asst. Tomogr.*, 1985, **9**, 659.
7. W. T. Dixon, *Radiology*, 1984, **153**, 189.
8. M. N. Hood, V. B. Ho, J. G. Smirniotopoulos, and J. Szumowski, *Radiographics*, 1999, **19**, 357.
9. P. A. Bottomley, T. H. Foster, and W. M. Leue, *Proc. Natl. Acad. Sci. U. S. A.*, 1984, **81**, 6856.
10. W. Block, J. M. Pauly, A. Kerr, and D. G. Nishimura, *Magn. Reson. Med.*, 1998, **40**, 194.
11. F. Schick, *Magn. Reson. Med.*, 1998, **40**, 194.
12. S. A. Mirowitz, *Am. J. Roentgenol.*, 1993, **161**, 1147.
13. J. Machann, O. P. Bachmann, K. Brechtel, D. B. Dahl, B. Wietek, B. Klumpp, H. U. Häring, C. D. Claussen, S. Jacob, and F. Schick, *J. Magn. Reson. Imaging*, 2003, **17**, 350.
14. F. Del Grande, F. Santini, D. A. Herzka, M. R. Aro, C. W. Dean, G. E. Gold, and J. A. Carrino, *Radiographics*, 2014, **34**, 217.
15. Q. Peng, R. W. McColl, J. Wang, J. M. Chia, and P. T. Weatherall, *J. Magn. Reson. Imaging*, 2005, **21**, 263.
16. S. Makrogiannis, S. Serai, K. W. Fishbein, C. Schreiber, L. Ferrucci, and R. G. Spencer, *J. Magn. Reson. Imaging*, 2012, **35**, 1152.
17. M. C. Raschpichler, I. Sorge, W. Hirsch, M. Mende, E. Sergeyev, D. Kruber, A. Koerner, and F. Schick, *Röfo*, 2012, **184**, 324.
18. J. Ma, *J. Magn. Reson. Imaging*, 2008, **28**, 543.
19. T. A. Bley, O. Wieben, C. J. François, J. H. Brittain, and S. B. Reeder, *J. Magn. Reson. Imaging*, 2010, **31**, 4.
20. H. Eggers and P. Börnert, *J. Magn. Reson. Imaging*, 2014, **40**, 251.
21. D. Hernando, Z. P. Liang, and P. Kellman, *Magn. Reson. Med.*, 2010, **64**, 811.
22. H. Yu, A. Shimakawa, C. D. Hines, C. A. McKenzie, G. Hamilton, C. B. Sirlin, J. H. Brittain, and S. B. Reeder, *Magn. Reson. Med.*, 2011, **66**, 199.
23. D. N. Costa, I. Pedrosa, C. McKenzie, S. B. Reeder, and N. M. Rofsky, *Am. J. Roentgenol.*, 2008, **190**, 1076.
24. C. B. Ahn, S. Y. Lee, O. Nalcioglu, and Z. H. Cho, *Magn. Reson. Imaging*, 1986, **4**, 110.
25. Q. S. Xiang, *Magn. Reson. Med.*, 2001, **9**, 789.
26. J. Ma, *J. Magn. Reson. Imaging*, 2008, **27**, 881.
27. Q. S. Xiang, *Magn. Reson. Med.*, 2006, **56**, 572.
28. H. Eggers, B. Brendel, A. Duijndam, and G. Herigault, *Magn. Reson. Med.*, 2011, **65**, 96.
29. J. Berglund, H. Ahlström, L. Johansson, and J. Kullberg, *Magn. Reson. Med.*, 2011, **65**, 994.
30. J. Ma, F. W. Wehrli, H. K. Song, and S. N. Hwang, *J. Magn. Reson.*, 1997, **125**, 92.
31. T. E. Skinner and G. H. Glover, *Magn. Reson. Med.*, 1997, **37**, 628.
32. G. H. Glover and E. Schneider, *Magn. Reson. Med.*, 1991, **18**, 371.
33. G. H. Glover, *J. Magn. Reson. Imaging*, 1991, **1**, 521.
34. A. R. Pineda, S. B. Reeder, Z. Wen, and N. J. Pelc, *Magn. Reson. Med.*, 2005, **54**, 625.
35. D. E. Horng, D. Hernando, C. D. Hines, and S. B. Reeder, *J. Magn. Reson. Imaging*, 2013, **37**, 414.
36. C. D. Hines, R. Agni, C. Roen, I. Rowland, D. Hernando, E. Bultman, D. Horng, H. Yu, A. Shimakawa, J. H. Brittain, and S. B. Reeder, *J. Magn. Reson. Imaging*, 2012, **35**, 844.
37. H. H. Hu and H. E. Kan, *NMR Biomed.*, 2013, **26**, 1609.
38. S. B. Reeder, H. H. Hu, and C. B. Sirlin, *J. Magn. Reson. Imaging*, 2012, **36**, 1011.
39. P. Peterson and S. Månsson, *Magn. Reson. Med.*, 2014, **71**, 219.
40. M. Bydder, T. Yokoo, G. Hamilton, M. S. Middleton, A. D. Chavez, J. B. Schwimmer, J. E. Lavine, and C. B. Sirlin, *Magn. Reson. Imaging*, 2008, **26**, 347.
41. S. Meisamy, C. D. Hines, G. Hamilton, C. B. Sirlin, C. A. McKenzie, H. Yu, J. H. Brittain, and S. B. Reeder, *Radiology*, 2011, **258**, 767.
42. C. Y. Liu, C. A. McKenzie, H. Yu, J. H. Brittain, and S. B. Reeder, *Magn. Reson. Med.*, 2007, **58**, 354.
43. I. Y. Wang, Y. Cui, C. N. Wiens, T. P. Wade, L. J. Friesen-Waldner, and C. A. McKenzie, *J. Magn. Reson. Imaging*, 2014, **39**, 217.
44. Q. S. Xiang and L. An, *J. Magn. Reson. Imaging*, 1997, **7**, 1002.
45. H. Yu, A. Shimakawa, C. A. McKenzie, E. Brodsky, J. H. Brittain, and S. B. Reeder, *Magn. Reson. Med.*, 2008, **60**, 1122.
46. J. Ren, I. Dimitrov, A. D. Sherry, and C. R. Malloy, *J. Lipid Res.*, 2008, **49**, 2055.
47. G. Hamilton, T. Yokoo, M. Bydder, I. Cruite, M. E. Schroeder, C. B. Sirlin, and M. S. Middleton, *NMR Biomed.*, 2011, **24**, 784.

48. X. Wang, D. Hernando, and S. B. Reeder, *Magn. Reson. Med.*, 2015. DOI: 10.1002/mrm.25681.

49. D. Hernando, C. D. Hines, H. Yu, and S. B. Reeder, *Magn. Reson. Med.*, 2012, **67**, 638.

50. D. Hernando, S. D. Sharma, H. Kramer, and S. B. Reeder, *Magn. Reson. Med.*, 2014, **72**, 646.

51. J. Berglund, H. Ahlström, and J. Kullberg, *Magn. Reson. Med.*, 2012, **68**, 1815.

52. P. Peterson and S. Månsson, *Magn. Reson. Med.*, 2013, **69**, 688.

Further Reading

B. Addeman, S. Kutty, T. G. Perkins, A. S. Soliman, C. N. Wiens, C. M. McCurdy, M. D. Beaton, R. A. Hegele, and C. A. McKenzie, *J. Magn. Reson. Imaging*, 2015, **41**, 233.

L. Arentsen, M. Yagi, Y. Takahashi, P. J. Bolan, M. White, D. Yee, and S. Hui, *Bone*, 2015, **72**, 118.

M. Bauwens, R. Wierts, B. Van Royen, J. Bucerius, W. Backes, F. Mottaghy, and B. Brans, *Eur. J. Nucl. Med. Mol. Imaging*, 2014, **41**, 776.

M. B. Bizino, M. L. Sala, P.de Heer, P.van der Tol, J. W. Smit, A. G. Webb, A.de Roos, and H. J. Lamb, *Magn. Reson. Imaging Clin. N. Am.*, 2015, **23**, 41.

P. Börnert, P. Koken, and H. Eggers, *J. Magn. Reson. Imaging*, 2010, **32**, 1262.

H. F. Brink, M. D. Buschmann, and B. R. Rosen, *Comput. Med. Imaging Graph.*, 1989, **13**, 93.

E. K. Brodsky, J. H. Holmes, H. Yu, and S. B. Reeder, *Magn. Reson. Med.*, 2008, **59**, 1151.

M. Bydder, O. Girard, and G. Hamilton, *Magn. Reson. Imaging*, 2011, **29**, 1041.

M. Bydder, T. Yokoo, H. Yu, M. Carl, S. B. Reeder, and C. B. Sirlin, *Magn. Reson. Imaging*, 2011, **29**, 216.

F. H. Cassidy, T. Yokoo, L. Aganovic, R. F. Hanna, M. Bydder, M. S. Middleton, A. D. Chavez, J. B. Schwimmer, and C. B. Sirlin, *Radiographics*, 2009, **29**, 231.

C. L. Dumoulin, *Magn. Reson. Med.*, 1985, **2**, 583.

R. Freeman and G. A. Morris, *J. Magn. Reson.*, 2011, **213**, 244.

J. W. Goldfarb, M. Roth, and J. Han, *Radiology*, 2009, **253**, 65.

D. Hernando, Y. S. Levin, C. B. Sirlin, and S. B. Reeder, *J. Magn. Reson. Imaging*, 2014, **40**, 1003.

K. G. Hollingsworth, P. L.de Sousa, V. Straub, and P. G. Carlier, *Neuromuscul. Disord.*, 2012, **22**, S54.

Y. Ishihara, A. Calderon, H. Watanabe, K. Okamoto, Y. Suzuki, K. Kuroda, and Y. Suzuki, *Magn. Reson. Med.*, 1995, **34**, 814.

D. M. Koh, M. Blackledge, S. Burns, J. Hughes, A. Stemmer, B. Kiefer, M. O. Leach, and D. J. Collins, *Eur. Radiol.*, 2012, **22**, 2648.

T. Lange, M. Buechert, M. W. Baumstark, P. Deibert, S. Gerner, H. Rydén, J. Seufert, and U. Korsten-Reck, *J. Magn. Reson. Imaging*, 2015. DOI: 10.1002/jmri.24919.

J. Li, Y. Xie, F. Yuan, B. Song, and C. Tang, *Pancreas*, 2011, **40**, 295.

Z. Li, C. Graff, A. F. Gmitro, S. W. Squire, A. Bilgin, E. K. Outwater, and M. I. Altbach, *Magn. Reson. Med.*, 2009, **61**, 1415.

M. E. Lidell, M. J. Betz, O. Dahlqvist Leinhard, M. Heglind, L. Elander, M. Slawik, T. Mussack, D. Nilsson, T. Romu, P. Nuutila, K. A. Virtanen, F. Beuschlein, A. Persson, M. Borga, and S. Enerbäck, *Nat. Med.*, 2013, **19**, 631.

C. Y. Liu, A. Redheuil, R. Ouwerkerk, J. A. Lima, and D. A. Bluemke, *Magn. Reson. Med.*, 2010, **63**, 892.

L. Lu, S. B. Donnola, M. Koontz, M. A. Griswold, J. L. Duerk, and C. A. Flask, *Magn. Reson. Med.*, 2015, **73**, 711.

W. Lu, H. Yu, A. Shimakawa, M. Alley, S. B. Reeder, and B. A. Hargreaves, *Magn. Reson. Med.*, 2008, **60**, 198.

U. A. Ludwig, F. Klausmann, S. Baumann, M. Honal, J. Hövener, D. König, P. Deibert, and M. Büchert, *J. Magn. Reson. Imaging*, 2014, **40**, 1437.

I. J. MacEwan, N. E. Glembotski, D. D'Lima, W. Bae, K. Masuda, H. H. Rashidi, L. K. Mell, and M. Bydder, *Magn. Reson. Imaging*, 2014, **32**, 1097.

J. Machann, A. Horstmann, M. Born, S. Hesse, and F. W. Hirsch, *Best Pract. Res. Clin. Endocrinol. Metab.*, 2013, **27**, 261.

A. J. Madhuranthakam, M. P. Smith, H. Yu, A. Shimakawa, N. M. Rofsky, C. A. McKenzie, and J. H. Brittain, *J. Magn. Reson. Imaging*, 2012, **35**, 1216.

C. H. Meyer, J. M. Pauly, A. Macovski, and D. G. Nishimura, *Magn. Reson. Med.*, 1990, **15**, 287.

C. J. Moran, E. K. Brdsky, L. H. Bancroft, S. B. Reeder, H. Yu, R. Kijowski, D. Engel, and W. F. Block, *Magn. Reson. Med.*, 2014, **71**, 95.

H. Moriguchi, J. S. Lewin, and J. L. Duerk, *Magn. Reson. Med.*, 2004, **52**, 1342.

L. Nardo, D. C. Karampinos, D. A. Lansdown, J. Carballido-Gamio, S. Lee, R. Maroldi, C. B. Ma, T. M. Link, and R. Krug, *J. Magn. Reson. Imaging*, 2014, **39**, 1178.

D. C. Noll, *IEEE Trans. Med. Imaging*, 1997, **16**, 372.

E. K. Outwater, R. Blasbalg, E. S. Siegelman, and M. Vala, *Radiographics*, 1998, **18**, 1465.

H. W. Park, D. J. Kim, and Z. H. Cho, *Magn. Reson. Med.*, 1987, **4**, 526.

N. S. Patel, M. R. Peterson, D. A. Brenner, E. Heba, C. Sirlin, and R. Loomba, *Aliment. Pharmacol. Ther.*, 2013, **37**, 630.

J. M. Rasmussen, S. Entringer, A. Nguyen, T. G. Van Erp, J. Burns, A. Guijarro, F. Oveisi, J. M. Swanson, D. Piomelli, P. D. Wadhwa, C. Buss, and S. G. Potkin, *PLoS One*, 2013, **30**, e77907.

S. B. Reeder, J. H. Brittain, T. M. Grist, and Y. F. Yen, *J. Magn. Reson. Imaging*, 2007, **26**, 1145.

S. B. Reeder, I. Cruite, G. Hamilton, and C. B. Sirlin, *J. Magn. Reson. Imaging*, 2011, **34**, 729.

M. D. Robson, P. D. Gatehouse, M. Bydder, and G. M. Bydder, *J. Comput. Assist. Tomogr.*, 2003, **27**, 825.

B. R. Rosen, V. J. Wedeen, and T. J. Brady, *J. Comput. Assist. Tomogr.*, 1984, **8**, 813.

J. Rydell, H. Knutsson, J. Pettersson, A. Johansson, G. Farnebäck, O. Dahlqvist, P. Lundberg, F. Nyström, and M. Borga, *Med. Image Comput. Comput. Assist. Interv.*, 2007, **10**, 210.

M. Schär, H. Eggers, N. R. Zwart, Y. Chang, A. Bakhru, and J. G. Pipe, *Magn. Reson. Med.*, 2015. DOI: 10.1002/mrm.25656.

S. D. Sharma, N. S. Artz, D. Hernando, D. E. Horng, and S. B. Reeder, *Magn. Reson. Med.*, 2015, **73**, 597.

J. Szumowski, W. R. Coshow, F. Li, and S. F. Quinn, *Radiology*, 1994, **192**, 555.

E. L. Thomas, J. A. Fitzpatrick, S. J. Malik, S. D. Taylor-Robinson, and J. D. Bell, *Prog. Nucl. Magn. Reson. Spectrosc.*, 2013, **73**, 53.

D. Thomasson, D. Purdy, and J. P. Finn, *Magn. Reson. Med.*, 1996, **35**, 563.

W. T. Triplett, C. Baligand, S. C. Forbes, R. J. Willcocks, D. J. Lott, S. DeVos, J. Pollaro, W. D. Rooney, H. L. Sweeney, C. G. Bönnemann, D. J. Wang, K. Vandenborne, and G. A. Walter, *Magn. Reson. Med.*, 2014, **72**, 8.

D. Wang, N. R. Zwart, Z. Li, M. Schär, and J. G. Pipe, *Magn. Reson. Med.*, 2015. DOI: 10.1002/mrm.25620.

H. Wang, Y. E. Chen, and D. T. Eitzman, *Arterioscler. Thromb. Vasc. Biol.*, 2014, **34**, 2217.

Y. Wang, D. Li, E. M. Haacke, and J. J. Brown, *J. Magn. Reson. Imaging*, 1998, **8**, 703.

F. Wiesinger, E. Wiedl, M. I. Menzel, M. A. Janich, O. Khegai, S. J. Glaser, A. Haase, M. Schwaiger, and R. F. Schulte, *Magn. Reson. Med.*, 2012, **68**, 8.

H. H. Wu, J. H. Lee, and D. G. Nishimura, *Magn. Reson. Med.*, 2008, **59**, 102.

T. Yokoo and J. D. Browning, *Top. Magn. Reson. Imaging*, 2014, **23**, 73.